This article has been accepted for publication in a future issue of this journal, but has not been fully edited. Content may change prior to final publication. Citation information: DOI 10.1109/TPWRS.2018.2820059, IEEE Transactions on Power Systems

A Generic Modeling and Power-Flow Analysis Approach for Isochronous and Droop-Controlled Microgrids

Mahmoud A. Allam, *Student Member, IEEE*; Amr. A. Hamad, *Member, IEEE;* and Mehrdad Kazerani, *Senior Member, IEEE*

***Abstract*—This paper proposes a generic steady-state modeling and power-flow analysis approach for droop- and isochronously-controlled microgrids. The proposed framework adopts symmetrical sequence component models, rather than phase-coordinate models, of microgrid elements. Such approach immensely reduces the power-flow execution time, as it breaks down the system model into independent equation sets with considerably reduced sizes. To render the proposed approach practical and generic, it integrates different types and control schemes of distributed generation (DG), including synchronous generator-based DG (SGDG) and electronically-interfaced DG (EIDG) units. Furthermore, it incorporates unbalanced loads and feeders, transformer connections, different load characteristics and configurations, as well as microgrid droop features. A novel power-flow algorithm based on a modified Newton-Raphson (NR) method is proposed to solve for the microgrid steady-state voltage magnitudes, angles, and frequency. The accuracy of the models and algorithm is verified through comparison with detailed time-domain simulations in MATALB/Simulink. Additionally, the proposed approach is shown to outperform the reported Newton-Trust Region (NTR) approach in generality, accuracy, and performance. Two case studies, incorporating IEEE 123-node test microgrid, are further performed to examine the effectiveness of the proposed approach in solving complicated droop-controlled microgrids, and to examine the behavior of droop-controlled DGs in isochronous microgrids.**

***Index Terms*— Distributed generation, droop control, isochronous, microgrids, power flow, unbalanced conditions.**

NOMENCLATURE

Acronyms:

DG	Distributed Generation
EIDG	Electronically-Interfaced Distributed Generation
ESS	Energy Storage System
NR	Newton Raphson
NTR	Newton-Trust Region
RER	Renewable Energy Resource
SGDG	Synchronous Generator-based Distributed Generation
VSC	Voltage Source Converter

Symbols:

$[B_{i,j}^{abc}]$	Shunt admittance matrix (3×3) of a feeder connecting nodes *i* and *j* in phase coordinated
$[Z_{ij}^{abc}]$	Series impedance matrix (3×3) of a feeder connecting nodes *i* and *j* in phase coordinated
$[T]$	Sequence component to phase coordinate transformation matrix (3×3)
$[B_{i,j}^{012}]$	Shunt admittance matrix (3×3) of a feeder connecting nodes *i* and *j* in sequence components
$[Y_{ij}^{012}]$	Series admittance matrix (3×3) of a feeder connecting nodes *i* and *j* in sequence components
V_i^x, V_j^x	Sequence component voltage at nodes *i* and *j*, respectively. $x \in \{0,1,2\}$
I_{ii}^x	Sequence component shunt admittance current due to a feeder connecting nodes *i* and *j*. $x \in \{0,1,2\}$
I_{ij}^x	Sequence component series admittance current due to a feeder connecting nodes *i* and *j*. $x \in \{0,1,2\}$
$\Delta I_{ii\_sh}^x$	Shunt admittance decoupling current due to a feeder connecting nodes *i* and *j*. $x \in \{0,1,2\}$
$\Delta I_{ij\_se}^x$	Series admittance decoupling current due to a feeder connecting nodes *i* and *j*. $x \in \{0,1,2\}$
$\Delta I_{i\_j}^x$	Combined series and shunt decoupling currents due to a feeder connecting nodes *i* and *j*. $x \in \{0,1,2\}$
$\Delta P_{i\_j}^1$, $\Delta Q_{i\_j}^1$	Positive-sequence decoupling active and reactive powers, respectively, at node *i* due to a feeder connecting nodes *i* and *j*
N	Number of microgrid nodes.
$[Y^{00}]$	Zero-sequence Y-bus matrix (*N*×*N*)
$[Y^{11}]$	Positive-sequence Y-bus matrix (*N*×*N*)
$[Y^{22}]$	Negative-sequence Y-bus matrix (*N*×*N*)
Y_{DG}^0, Y_{DG}^2	DG's zero- and negative-sequence admittances, respectively
R_a	SGDG's phase resistance
R_n, X_n	SGDG's neutral resistance and reactance, respectively
$X''_{d-unsat}$, $X''_{q-unsat}$	SGDG's unsaturated direct and quadrature axis sub-transient reactances, respectively
$P_{G,i}^1, Q_{G,i}^1$	DG's positive-sequence active and reactive powers, respectively, at node *i*
$\omega_{0,i}$	DG's no-load angular frequency
ω	DG/Microgrid's angular frequency
$V_{0,i}^1$	DG's positive-sequence no-load voltage magnitude
η_i, μ_i	DG's active and reactive power droop gains, respectively
$P_{G,i}^{max}$, $Q_{G,i}^{max}$	DG's maximum active and reactive powers, respectively
ω_{max}, ω_{min}	DG's maximum and minimum angular frequencies, respectively
V_{max}^1, V_{min}^1	DG's maximum and minimum positive-sequence output voltage magnitudes, respectively
V_Δ^x, V_Y^x	Transformer sequence component voltages at the delta- and Y-connected sides, respectively $x \in \{0,1,2\}$
I_Δ^x, I_Y^x	Transformer sequence component currents at the

M. A. Allam and M. Kazerani are with the Department of Electrical and Computer Engineering at the University of Waterloo, Waterloo, ON N2L 3G1, Canada.

Amr A. Hamad is a research associate with National Research Council Canada (NRC-CNRC), Ottawa, ON K1A 0R6, Canada (email: amr.said@nrc-cnrc.gc.ca).

This article has been accepted for publication in a future issue of this journal, but has not been fully edited. Content may change prior to final publication. Citation information: DOI 10.1109/TPWRS.2018.2820059, IEEE Transactions on Power Systems

	delta- and Y-connected sides, respectively $x \in \{0,1,2\}$
$Y_{s.c}$	Transformer short-circuit admittance
P_{G,i_sp}, Q_{G,i_sp}	Grid-tied DG's specified active and reactive powers, respectively
V_{i_sp}	Grid-tied DG's specified voltage magnitude
$V_{L,i}^{x}, I_{L,i}^{x}$	Load phase voltage and current, respectively $x \in \begin{cases}\{a,b,c\} & for\ Y\ loads \\ \{ab,bc,ca\} & for\ \Delta\ loads\end{cases}$
$P_{L,i}^{x}, Q_{L,i}^{x}$	Load phase active and reactive powers, respectively $x \in \begin{cases}\{a,b,c\} & for\ Y\ loads \\ \{ab,bc,ca\} & for\ \Delta\ loads\end{cases}$
$P_{L,i}^{0,x}, Q_{L,i}^{0,x}$	Nominal load phase active and reactive powers, respectively $x \in \begin{cases}\{a,b,c\} & for\ Y\ loads \\ \{ab,bc,ca\} & for\ \Delta\ loads\end{cases}$
$\alpha_i^{x}, \beta_i^{x}$	Load active and reactive power-voltage exponents, respectively $x \in \begin{cases}\{a,b,c\} & for\ Y\ loads \\ \{ab,bc,ca\} & for\ \Delta\ loads\end{cases}$
$K_{pf,i}^{x}, K_{qf,i}^{x}$	Load active and reactive power-frequency constants, respectively $x \in \begin{cases}\{a,b,c\} & for\ Y\ loads \\ \{ab,bc,ca\} & for\ \Delta\ loads\end{cases}$
$\Delta\omega$	Angular frequency deviation from its nominal value
$I_{L,i}^{x}$	Sequence component line load current. $x \in \{0,1,2\}$
$P_{L,i}^{1}, Q_{L,i}^{1}$	Load positive-sequence active and reactive powers, respectively
λ	Loading factor
$P_{L,i\_base}^{0,x}$, $Q_{L,i\_base}^{0,x}$	Base values of the nominal load phase active and reactive powers, respectively $x \in \begin{cases}\{a,b,c\} & for\ Y\ loads \\ \{ab,bc,ca\} & for\ \Delta\ loads\end{cases}$
$\Delta\mathcal{P}_i^{1}, \Delta Q_i^{1}$	Positive-sequence active and reactive power mismatches, respectively, at node *i*
P_i^{1}, Q_i^{1}	Injected positive-sequence active and reactive powers, respectively, at node *i*
$\delta_i^{1}, \delta_j^{1}$	Positive-sequence voltage angles at nodes *i* and *j*, respectively
Y_{ii}^{11}, Y_{ij}^{11}	Positive-sequence Y-Bus self and mutual admittance magnitudes, respectively
$\theta_{ii}^{11}, \theta_{ij}^{11}$	Positive-sequence Y-Bus self and mutual admittance angles, respectively
$\|\boldsymbol{V^1}\|$	Positive-sequence voltage magnitude vector (*N×1*)
$\boldsymbol{\delta^1}$	Positive-sequence voltage angle vector (*N-1×1*)
$\Delta\boldsymbol{\mathcal{P}^1}, \Delta\boldsymbol{Q^1}$	Active and reactive power mismatch vectors (*N×1*).
$[J]$	Jacobian matrix (*N×N*)
$\Delta I_i^{0}, \Delta I_i^{2}$	Total zero- and negative-sequence decoupling currents, respectively, at node *i* due to all feeders connected to the node
$\Delta\boldsymbol{I^0}, \Delta\boldsymbol{I^2}$	Zero- and negative-sequence decoupling current vectors (*N×1*), respectively
$\boldsymbol{I_L^0}, \boldsymbol{I_L^2}$	Zero- and negative-sequence load current vectors (*N×1*), respectively
$\boldsymbol{V^0}, \boldsymbol{V^2}$	Zero- and negative-sequence voltage vectors (*N×1*), respectively
$\|\blacksquare\|$	Variable's magnitude

I. Introduction

Motivation for green, efficient, sustainable and reliable electrical networks has led to introduction of microgrids as a viable paradigm for power delivery [1]. The existence of distributed generators (DGs) close to load centers, as implied in microgrid concept, potentially reduces power loss in the transmission stage, and increases the cultivation of local renewable energy resources (RERs) and energy storage systems (ESSs). Microgrids also provide a new reliability dimension by allowing autonomous operation of distribution systems in islanded mode during grid faults [2], and in isolated mode due to lack of access to bulk power systems in remote communities [3]. The analysis of islanded and isolated microgrids is more challenging than that of grid-connected ones, in which voltage and frequency are regulated by a stiff grid. The research is still ongoing to provide accurate analysis tools that describe microgrids' steady-state and dynamic behaviors.

For several decades, synchronous generator-based DGs (SGDGs), such as diesel and gas generator-sets, have played a vital role in powering isolated electrical distribution networks [3]. Furthermore, these generators are commonly integrated to grid-connected distribution systems to export power or to provide a stand-by source in case of the main grid's outage, thus forming an islanded microgrid. On the other hand, the enormous benefits of advanced electronically-interfaced DGs (EIDGs), such as flexibility, speed, and interfacing RERs, urge their integration into modern distribution networks. Accordingly, both types of DGs are anticipated to coexist in microgrids [4]. Research is ongoing on the dynamic behavior of networks that comprise the two types of DGs [5]. However, their steady-state performance has not been yet investigated.

Power-flow analysis tools play a key role in planning and operation studies of electrical power systems. At the transmission level, various power-flow algorithms have been established to analyze balanced bulk power systems [6]. Some of these algorithms have been further extended to include unbalanced operation [7]. At the active distribution level, some power-flow algorithms have been developed for grid-connected microgrids with integrated DGs, where a stiff grid acts as an ideal slack bus maintaining balanced voltages with fixed magnitude and frequency at the source node [8]. However, this analysis does not consider the integration of droop-controlled DGs, which can potentially be used in grid-connected mode to allow autonomous operation of islanded microgrids formed after an islanding event [2]. Additionally, the analysis does not account for unbalances at the source node in case the primary source is not ideal, such as in isolated SGDG-fed microgrids.

Moreover, some approaches employ different strategies to account for microgrids' droop features. Characterized by their load-dependent voltage magnitude and frequency, droop-controlled ac microgrids differ from conventional ac systems discussed above in the following aspects: (i) droop-controlled microgrids lack a slack bus; (ii) the microgrid's frequency is a power-flow variable; and (iii) the feeder and load models are frequency-dependent. Altogether, these characteristics complicate the power-flow problem formulation and solution, as compared to conventional distribution networks. In [9] and [10], modified Newton Raphson (NR) approaches have been introduced by providing additional mismatch equations and Jacobian matrix elements that accommodate the system's droop characteristics. Similarly, a forward-backward approach has been proposed in [11] for droop-controlled microgrids. Nevertheless, the application of these methods is limited to balanced microgrids. The authors of [12] have proposed a power-flow algorithm based on a Newton-Trust Region (NTR) method to solve the unbalanced microgrid's set of frequency-dependent nonlinear equations in phase-coordinates. However, the authors have not considered SGDGs in their study,

This article has been accepted for publication in a future issue of this journal, but has not been fully edited. Content may change prior to final publication. Citation information: DOI 10.1109/TPWRS.2018.2820059, IEEE Transactions on Power Systems

which are challenging to model in phase-coordinates, considering the machines' saliency and internal impedances [8]. Furthermore, their models ignore the influence of the interfacing transformer's delta/wye connection on the EIDG phase loading and voltage unbalances. In addition to its high computational cost, this approach does not include some aspects, such as shunt admittances of distribution feeders and delta-connected loads that commonly exist in distribution systems [13].

This paper proposes a generic power-flow algorithm for droop-controlled and isochronous microgrids under unbalanced conditions. The algorithm incorporates the sequence component models – rather than phase coordinate models used in [12] – of all system components, including various types of DG units with different steady-state characteristics. The adopted models allow for precise representations of SGDGs, as well as different configurations and controls of EIDGs [14]. The proposed algorithm utilizes these sequence component models to break down the steady-state analysis into three smaller independent, yet correlated, sub-problems. Accordingly, this method significantly reduces the power-flow execution time with respect to NTR methods, as it deals with a set of small matrices rather than one large matrix representing the system as a whole.

Based on the above-identified limitations of the power-flow approaches reported in the literature, the contribution of this work can be summarized as follows: 1) developing a generic, accurate, and computationally-efficient power-flow analysis approach, 2) integrating different DG types and various aspects of droop-controlled and isochronous unbalanced microgrids, which have not been considered in previous studies, and 3) inspecting the operation of droop-controlled DGs in unbalanced isochronous microgrids.

The remainder of the paper is organized as follows: Section II sheds lights on different operational modes of islanded and isolated microgrids. Section III describes the steady-state sequence-component mathematical modeling of microgrid elements. The proposed power-flow algorithm is explained in Section IV. Section V attests the validity of the proposed algorithm, and section VI investigates the introduced approach and the microgrid operation through case studies. Finally, Section VII concludes the paper.

II. Operational Modes of Microgrids

Numerous factors affect the operational mode of a microgrid, among which microgrid size, availability of RERs, access to fuel, types of loads, and various economic considerations are significant [15]. A large DG may operate isochronously to set the microgrid's frequency, whereas a group of DGs with relatively similar capacities may employ droop controllers to collaboratively set the microgrid's voltage and frequency. Hence, microgrids can be categorized as droop-controlled and isochronously-controlled.

A. Droop-Controlled Microgrids

Droop controls are typically adopted to allow proportional power sharing among generators with comparable capacities. Thus, SGDGs could be droop-controlled at the primary level along with other EIDGs in islanded microgrids if they have close capacities. In this context, the microgrid's voltage magnitude and frequency are load-dependent. It is worth mentioning that a low-bandwidth supervisory controller is potentially required to monitor and regulate system variables (i.e., microgrid's voltage magnitude and frequency), especially if the microgrid supplies sensitive and critical loads. However, lack of a slack bus and proportional power sharing among the DGs eliminate system's dependence on one generator, which potentially increases the microgrid's autonomy and reliability. This scheme could be desirable in islanded microgrids that normally operate in grid-connected mode.

B. Isochronously-Controlled Microgrids

In this mode, a dominant DG – typically SGDG – is operated in isochronous mode, thereby functioning as a slack bus (i.e., maintaining constant frequency and voltage at its terminals regardless of the connected load). Other DGs can inject active and reactive powers to the microgrid while following the main SGDG's frequency. It is noteworthy that this case is similar to the grid-connected mode of operation where the connection with the grid operates as a slack bus. However, the synchronous generator cannot keep its terminal voltages balanced under unbalanced loading due to its internal impedances, and thus it is not considered an ideal slack bus. Although the dominant SGDG forms the microgrid's voltage, other dispatchable DGs can still adopt droop controls to sustain the microgrid operation in case of failure of the main SGDG. The output powers of these DGs are controlled by adjusting their droop settings, which is attainable through a higher level secondary controller. Non-dispatchable DGs – typically EIDGs – can inject powers to the microgrid, yet they cannot form the microgrid voltage for proper operation if the main DG fails. This scheme is most suitable for isolated microgrids where DGs are to be integrated into existing gas- or diesel-powered networks.

III. Microgrid Modeling in Sequence Components

Unlike ac transmission systems, ac distribution networks are predominantly unbalanced due to the networks intrinsic features, such as the existence of single-phase DGs and loads, feeder configurations, and single- and two-phase distribution laterals. This imbalance imposes further challenges on microgrids' modeling and analysis. A symmetrical sequence component analysis is therefore employed in this study for accurate representation of all microgrid components under unbalanced conditions.

A. Feeder Modeling

Distribution networks typically adopt 4-wire three-phase feeders, commonly unbalanced and untransposed, in addition to single- and/or two-phase laterals. Thus, the impedance matrix $\left[Z_{ij}^{abc}\right]$ between any two nodes i and j, and the shunt admittance matrix $\left[B_{i,j}^{abc}\right]$ are asymmetrical in the phase form. The sequence component series admittance matrix can, hence, be calculated as

$$\left[Y_{ij}^{012}\right] = [T]^{-1}\left[Z_{ij}^{abc}\right]^{-1}[T] = \begin{bmatrix} y_{ij}^{00} & y_{ij}^{01} & y_{ij}^{02} \\ y_{ij}^{10} & y_{ij}^{11} & y_{ij}^{12} \\ y_{ij}^{20} & y_{ij}^{21} & y_{ij}^{22} \end{bmatrix} \quad (1)$$

where 0, 1 and 2 stand for zero-, positive- and negative-sequence components, respectively, and

$$[T] = \begin{bmatrix} 1 & 1 & 1 \\ 1 & a^2 & a \\ 1 & a & a^2 \end{bmatrix} \quad \text{where} \quad a = 1\angle 120°$$

Similarly, the shunt admittance matrix can be obtained in the sequence component frame as

$$\left[B_{i,j}^{012}\right] = [T]^{-1}\left[B_{i,j}^{abc}\right][T] = \begin{bmatrix} b_{i,j}^{00} & b_{i,j}^{01} & b_{i,j}^{02} \\ b_{i,j}^{10} & b_{i,j}^{11} & b_{i,j}^{12} \\ b_{i,j}^{20} & b_{i,j}^{21} & b_{i,j}^{22} \end{bmatrix} \quad (2)$$

Since the phase matrices are asymmetrical, the sequence component admittance matrices are not symmetric diagonal, which implies that the three sequence components are coupled.

This article has been accepted for publication in a future issue of this journal, but has not been fully edited. Content may change prior to final publication. Citation information: DOI 10.1109/TPWRS.2018.2820059, IEEE Transactions on Power Systems

Considering the series admittance matrix, given by (1), the sequence component currents flowing through the feeder connecting nodes *i* and *j* are given by

$$\begin{bmatrix} I_{ij}^0 \\ I_{ij}^1 \\ I_{ij}^2 \end{bmatrix} = \begin{bmatrix} y_{ij}^{00} & y_{ij}^{01} & y_{ij}^{02} \\ y_{ij}^{10} & y_{ij}^{11} & y_{ij}^{12} \\ y_{ij}^{20} & y_{ij}^{21} & y_{ij}^{22} \end{bmatrix} \begin{bmatrix} V_i^0 - V_j^0 \\ V_i^1 - V_j^1 \\ V_i^2 - V_j^2 \end{bmatrix} \quad (3)$$

By introducing series admittance decoupling currents, $[\Delta I_{ij\_se}^{012}]$, defined by (4), the three sequence currents can be decoupled as illustrated in (5).

$$\begin{bmatrix} \Delta I_{ij\_se}^0 \\ \Delta I_{ij\_se}^1 \\ \Delta I_{ij\_se}^2 \end{bmatrix} = \begin{bmatrix} 0 & y_{ij}^{01} & y_{ij}^{02} \\ y_{ij}^{10} & 0 & y_{ij}^{12} \\ y_{ij}^{20} & y_{ij}^{21} & 0 \end{bmatrix} \begin{bmatrix} V_i^0 - V_j^0 \\ V_i^1 - V_j^1 \\ V_i^2 - V_j^2 \end{bmatrix} \quad (4)$$

$$\begin{bmatrix} I_{ij}^0 \\ I_{ij}^1 \\ I_{ij}^2 \end{bmatrix} = \begin{bmatrix} y_{ij}^{00} & 0 & 0 \\ 0 & y_{ij}^{11} & 0 \\ 0 & 0 & y_{ij}^{22} \end{bmatrix} \begin{bmatrix} V_i^0 - V_j^0 \\ V_i^1 - V_j^1 \\ V_i^2 - V_j^2 \end{bmatrix} + \begin{bmatrix} \Delta I_{ij\_se}^0 \\ \Delta I_{ij\_se}^1 \\ \Delta I_{ij\_se}^2 \end{bmatrix} \quad (5)$$

Similarly, the shunt admittance matrix, defined by (2), introduces coupled sequence component currents injected at node *i* as

$$\begin{bmatrix} I_{ii}^0 \\ I_{ii}^1 \\ I_{ii}^2 \end{bmatrix} = j \begin{bmatrix} b_{i,j}^{00} & b_{i,j}^{01} & b_{i,j}^{02} \\ b_{i,j}^{10} & b_{i,j}^{11} & b_{i,j}^{12} \\ b_{i,j}^{20} & b_{i,j}^{21} & b_{i,j}^{22} \end{bmatrix} \begin{bmatrix} V_i^0 \\ V_i^1 \\ V_i^2 \end{bmatrix} \quad (6)$$

The shunt injected currents can also be decoupled if shunt decoupling currents, $[\Delta I_{ii\_sh}^{012}]$, are introduced as

$$\begin{bmatrix} \Delta I_{ii\_sh}^0 \\ \Delta I_{ii\_sh}^1 \\ \Delta I_{ii\_sh}^2 \end{bmatrix} = j \begin{bmatrix} 0 & b_{i,j}^{01} & b_{i,j}^{02} \\ b_{i,j}^{10} & 0 & b_{i,j}^{12} \\ b_{i,j}^{20} & b_{i,j}^{21} & 0 \end{bmatrix} \begin{bmatrix} V_i^0 \\ V_i^1 \\ V_i^2 \end{bmatrix} \quad (7)$$

Hence, the sequence currents injected due to the feeder shunt admittance can be decoupled using (8).

$$\begin{bmatrix} I_{ii}^0 \\ I_{ii}^1 \\ I_{ii}^2 \end{bmatrix} = j \begin{bmatrix} b_{i,j}^{00} & 0 & 0 \\ 0 & b_{i,j}^{11} & 0 \\ 0 & 0 & b_{i,j}^{22} \end{bmatrix} \begin{bmatrix} V_i^0 \\ V_i^1 \\ V_i^2 \end{bmatrix} + \begin{bmatrix} \Delta I_{ii\_sh}^0 \\ \Delta I_{ii\_sh}^1 \\ \Delta I_{ii\_sh}^2 \end{bmatrix} \quad (8)$$

Therefore, complete decoupling between different sequence frames can be realized using current decoupling components, $[\Delta I_{i\_j}^{012}]$, that comprise both series and shunt decoupling currents, as given in (9).

$$\begin{bmatrix} \Delta I_{i\_j}^0 \\ \Delta I_{i\_j}^1 \\ \Delta I_{i\_j}^2 \end{bmatrix} = \begin{bmatrix} \Delta I_{ij\_se}^0 \\ \Delta I_{ij\_se}^1 \\ \Delta I_{ij\_se}^2 \end{bmatrix} + \begin{bmatrix} \Delta I_{ii\_sh}^0 \\ \Delta I_{ii\_sh}^1 \\ \Delta I_{ii\_sh}^2 \end{bmatrix} \quad (9)$$

Furthermore, since positive-sequence power-flow analysis deals with active and reactive powers rather than currents, the positive-sequence decoupling component is transformed from current into power by applying

$$\Delta P_{i\_j}^1 + \Delta Q_{i\_j}^1 = V_i^1 \left(\Delta I_{i\_j}^1\right)^* \quad (10)$$

Finally, the decoupling current/power components can be formulated in their complete forms as (11)-(13).

Consequently, three decoupled Y-bus matrices – $[Y^{00}]$, $[Y^{11}]$, and $[Y^{22}]$ – can be constructed to formulate the three sequence

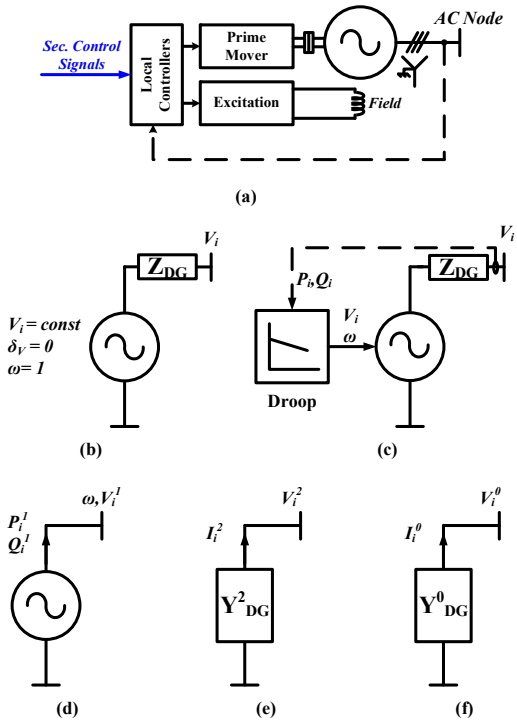

Fig. 1. Schematic diagram and models of SGDG

component power-flow problems independently. It is noteworthy that, unlike in grid-connected systems, the admittance matrices' parameters are load-dependent in droop controlled microgrids [12]. This fact necessitates updating the admittance matrices' elements according to the microgrid's frequency, which complicates the power-flow problem.

B. DG Modeling

The physical structures of different DGs along with their various control schemes imply different mathematical models to precisely represent each DG type. DGs can mostly be classified into four categories as discussed in the following subsections. Note that other DG types can be modeled following the same approach.

1) Droop-controlled SGDG

Although various SGDGs adopt similar primary circuit configurations, as shown in Fig. 1 (a), their models slightly vary based on their control schemes. Assuming that the SGDG regulates the positive sequence voltage at its terminals, the positive-sequence DG model can be represented as depicted in Fig. 1 (d) [8]. Furthermore, the negative and zero sequence component circuits can be modeled as shown in Figs. 1 (e) and (f), respectively, where the circuit admittances are obtained from the generator's datasheet or calculated using [16]

$$Y_{DG}^2 = [R_a + j\frac{X''_{d-unsat} + X''_{q-unsat}}{2}]^{-1} \quad (14)$$

$$Y_{DG}^0 = [R_a + 3R_n + j(\frac{X''_{d-unsat} + X''_{q-unsat}}{8} + 3X_n)]^{-1} \quad (15)$$

where R_a is the armature resistance, $X''_{d-unsat}$ and $X''_{q-unsat}$ are the unsaturated direct and quadrature axes sub-transient reactances respectively, and R_n and X_n are the neutral resistance and reactance, respectively. Although SGDG generates balanced

$$\Delta I_{i\_j}^0 = \left[y_{ij}^{01}\left(V_i^1 - V_j^1\right) + y_{ij}^{02}\left(V_i^2 - V_j^2\right)\right] + \left[jb_{i,j}^{01}V_i^1 + jb_{i,j}^{02}V_i^2\right] \quad (11)$$

$$\Delta P_{i\_j}^1 + \Delta Q_{i\_j}^1 = V_i^1 \left[\left[y_{ij}^{10}\left(V_i^0 - V_j^0\right) + y_{ij}^{12}\left(V_i^2 - V_j^2\right)\right] + \left[jb_{i,j}^{10}V_i^0 + jb_{i,j}^{12}V_i^2\right]\right]^* \quad (12)$$

$$\Delta I_{i\_j}^2 = \left[y_{ij}^{21}\left(V_i^1 - V_j^1\right) + y_{ij}^{20}\left(V_i^0 - V_j^0\right)\right] + \left[jb_{i,j}^{20}V_i^0 + jb_{i,j}^{21}V_i^1\right] \quad (13)$$

This article has been accepted for publication in a future issue of this journal, but has not been fully edited. Content may change prior to final publication. Citation information: DOI 10.1109/TPWRS.2018.2820059, IEEE Transactions on Power Systems

positive-sequence internal electromotive force (EMF), its terminal voltage undergoes unbalances under unequal phase loadings. The voltages across the negative and zero sequence admittances represent the voltage unbalance at the terminals.

As shown in Fig. 1 (c), a droop-controlled SGDG's output voltage magnitude and frequency are dependent on the output powers, as governed by the droop equations

$$P^1_{G,i} = \frac{1}{3}\eta_i\,(\omega_{0,i} - \omega) \tag{16}$$

$$Q^1_{G,i} = \frac{1}{3}\,\mu_i(V^1_{0,i} - |V^1_i|\,) \tag{17}$$

where the droop gains η_i and μ_i are typically set as

$$\eta_i = \frac{P^{max}_{G,i}}{\omega_{max} - \omega_{min}} \tag{18}$$

$$\mu_i = \frac{Q^{max}_{G,i}}{V^1_{max} - V^1_{min}} \tag{19}$$

In (18) and (19), $P^{max}_{G,i}$ and $Q^{max}_{G,i}$ are the DG's maximum active and reactive powers, respectively, ω_{max} and ω_{min} are the microgrid's maximum and minimum allowed frequencies, respectively, and V^1_{max} and V^1_{min} are the DG's maximum and minimum positive-sequence terminal voltages, respectively. It is essential to mention that the SGDG's negative- and zero- sequence admittances, Y^2_{DG} and Y^0_{DG}, are not constant, since the DGs' reactances are reliant on the load-dependent system frequency ω.

2) Isochronously-controlled SGDG

An isochronously-controlled SGDG is able to fix the microgrid's frequency while regulating the voltage at its terminals to a constant value. It can, thus, be considered a "non-ideal" slack bus. To model this DG, the same models and droop equations presented above can still be adopted by setting the droop gains to infinity. The SGDG's set-points (i.e., ω_0 and V^1_0) will determine the microgrid's frequency and the DG's terminal voltage, as shown in Fig. 1 (b). The SGDG's admittances are no longer variable in this case.

3) Droop-controlled EIDG

Voltage-source converter (VSC)-based EIDGs, Fig. 2 (a), can also implement droop controls to contribute in forming the microgrid voltage, as depicted in Fig. 2 (b). In contrast with SGDGs, they can suppress negative-sequence voltages at their terminals by implementing proper control loops, which denotes infinity negative-sequence admittance, as shown in Fig. 2 (e) [17]. However, other negative-sequence controls can also be adopted to realize negative-sequence current sharing among EIDGs [18]. Moreover, EIDGs can incorporate different circuit configurations, which primarily affect the DG's zero-sequence model. DGs that implement 3-leg VSCs do not provide a neutral current path; thus, they are represented as open circuit in the zero-sequence frame, as depicted in Fig. 2 (f). However, 4-leg VSCs provide a neutral wire interfaced to the fourth leg through a filtering inductor. Therefore, their zero-sequence circuit is modeled as a short circuit if the VSC's controllers maintain balanced terminal voltages, or as a finite admittance otherwise, as shown in Fig. 2 (g). It is worth mentioning that 3-leg VSCs are often interfaced to the 4-wire network through delta/grounded-wye transformers. With this configuration, the transformer's model, given by (20), must be

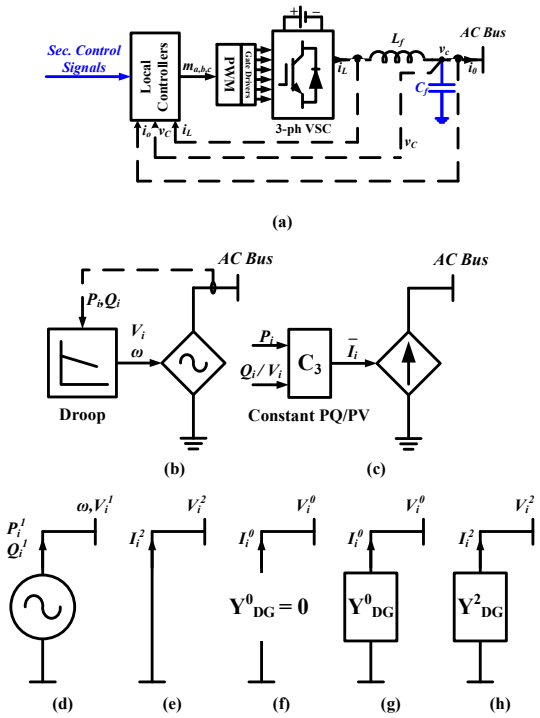

Fig. 2. Schematic diagram and models of EIDGs.

integrated into the EIDG's model [19]. The previously presented droop equations (16)-(19) are valid for all discussed configurations of EIDGs.

4) Grid-Tied EIDG (Constant PQ/PV EIDG)

EIDGs may employ a grid-tied control scheme, which is typical for intermittent and non-dispatchable sources. In this control topology, the EIDG often employs a current-controlled VSC that does not contribute to forming the grid voltage; instead, it synchronizes to the existing grid and acts as a grid-follower (i.e., grid-tied) [14]. The EIDG injects controlled currents, as illustrated in Fig. 2 (c), to follow the DG's power or voltage references.

In the positive-sequence frame, a constant PQ EIDG is modeled as constant active and reactive power source, given by

$$P^1_{G,i} = \frac{1}{3}\,P_{G,i\_sp} \tag{21}$$

$$Q^1_{G,i} = \frac{1}{3}\,Q_{G,i\_sp} \tag{22}$$

where P_{G,i_sp} and Q_{G,i_sp} are the EIDG's specified active and reactive powers. Alternatively, a constant PV EIDG can regulate the node voltage, rather than injecting constant reactive power, and henceforth it can be represented by (21) and (23).

$$|V^1_i| = V_{i\_sp} \tag{23}$$

Other grid-tied EIDG control schemes can also be represented by introducing minor modifications to (21)-(22).

On the other hand, the EIDG is represented as admittances in the zero- and negative-sequence models, as shown in Fig. 2 (g) and (h), respectively. The zero- and negative sequence admittances can have zero, infinite, or finite nonzero values. Such values are dependent on the converter's structure (i.e., 3-leg or 4-leg), output filter configuration, and EIDG's control scheme, as described in

$$\begin{bmatrix} I^0_\Delta \\ I^1_\Delta \\ I^2_\Delta \\ I^0_Y \\ I^1_Y \\ I^2_Y \end{bmatrix} = \begin{bmatrix} 0 & 0 & 0 & 0 & 0 & 0 \\ 0 & Y_{s.c} & 0 & 0 & -Y_{s.c}\angle -30 & 0 \\ 0 & 0 & Y_{s.c} & 0 & 0 & -Y_{s.c}\angle 30 \\ 0 & 0 & 0 & Y_{s.c} & 0 & 0 \\ 0 & -Y_{s.c}\angle 30 & 0 & 0 & Y_{s.c} & 0 \\ 0 & 0 & -Y_{s.c}\angle -30 & 0 & 0 & Y_{s.c} \end{bmatrix} \begin{bmatrix} V^0_\Delta \\ V^1_\Delta \\ V^2_\Delta \\ V^0_Y \\ V^1_Y \\ V^2_Y \end{bmatrix} \tag{20}$$

This article has been accepted for publication in a future issue of this journal, but has not been fully edited. Content may change prior to final publication. Citation information: DOI 10.1109/TPWRS.2018.2820059, IEEE Transactions on Power Systems

[8] and [20]. It is noteworthy that although the same EIDG models in [8] and [20] for grid-connected microgrids can be adopted in the proposed work, the frequency dependency of the EIDGs' admittances has to be taken into consideration in this study.

C. Load Modeling

The steady-state model of loads is primarily dependent on their type. Loads are affected differently by voltage and frequency deviations that typically occur in droop-controlled microgrids. The load features are incorporated in this study through a generic static load model that reflects the load's dependency on voltage and frequency [21]:

$$P_{L,i}^{x} = P_{L,i}^{0,x} \left|V_{L,i}^{x}\right|^{\alpha_i^x} (1 + K_{pf,i}^{x}\,\Delta\omega) \tag{24}$$

$$Q_{L,i}^{x} = Q_{L,i}^{o,x} \left|V_{L,i}^{x}\right|^{\beta_i^x} (1 + K_{qf,i}^{x}\,\Delta\omega) \tag{25}$$

where P_L^o and Q_L^o are the nominal load active and reactive powers, α and β the active and reactive power exponents, $\Delta\omega$ the frequency deviation, and K_{pf} and K_{qf} the constants defining the load dependency on frequency deviations [21]. The values of the power exponents α and β are sometimes equal, and take the values of 0, 1, or 2 for constant-power, constant-current, and constant-impedance loads, respectively. They, however, may be assigned different values to represent other load types if needed. On the other hand, the values of K_{pf} and K_{qf} vary with the load class (i.e., residential, commercial, etc.) and season (i.e., summer, winter … etc.). At the lower power level, the load components (i.e., air conditioner, heater, television, etc.) contribute to these values. Further details on various load types and their dependencies on voltage and frequency can be found in [21] and [22].

Since loads in distribution systems are typically unbalanced, the currents of load phases must be calculated individually:

$$I_{L,i}^{x} = \frac{P_{L,i}^{x} - jQ_{L,i}^{x}}{V_{L,i}^{x\,*}} \tag{26}$$

$$\text{where } x \in \begin{cases} \{a,b,c\} & for\ Y\ loads \\ \{ab,bc,ca\} & for\ \Delta\ loads \end{cases}$$

The load currents can, then, be transformed into their respective sequence components by applying

$$\begin{bmatrix} I_{L,i}^{0} \\ I_{L,i}^{1} \\ I_{L,i}^{2} \end{bmatrix} = [T]^{-1} \begin{bmatrix} I_{L,i}^{a} \\ I_{L,i}^{b} \\ I_{L,i}^{c} \end{bmatrix} \tag{27}$$

The positive-sequence load active and reactive powers can, therefore, be calculated as

$$P_{L,i}^{1} + Q_{L,i}^{1} = V_i^{1}(I_{L,i}^{1})^{*} \tag{28}$$

While (26)-(28) can directly be applied to Y-connected loads, Δ-connected loads require more attention, as they encounter line voltages. Conversions between line and phase quantities, through (29)-(30), are necessary before substituting into (26)-(28).

$$\begin{bmatrix} V_{L,i}^{ab} \\ V_{L,i}^{bc} \\ V_{L,i}^{ca} \end{bmatrix} = \begin{bmatrix} 1 & -1 & 0 \\ 0 & 1 & -1 \\ -1 & 0 & 1 \end{bmatrix} \begin{bmatrix} V_{L,i}^{a} \\ V_{L,i}^{b} \\ V_{L,i}^{c} \end{bmatrix} \tag{29}$$

$$\begin{bmatrix} I_{L,i}^{a} \\ I_{L,i}^{b} \\ I_{L,i}^{c} \end{bmatrix} = \begin{bmatrix} 1 & 0 & -1 \\ -1 & 1 & 0 \\ 0 & -1 & 1 \end{bmatrix} \begin{bmatrix} I_{L,i}^{ab} \\ I_{L,i}^{bc} \\ I_{L,i}^{ca} \end{bmatrix} \tag{30}$$

IV. Proposed Power-Flow Algorithm

Obtaining a generic and accurate steady-state solution for droop-controlled microgrids is cumbersome if the problem is formulated in phase-coordinates. The decomposition into sequence components provides a more flexible and accurate alternative for modeling different operational modes of DGs and the inherent unbalanced feature of microgrids. In this work, the sequence component approach is adopted to solve the power-flow of microgrids that comprise different DG types. As illustrated in Fig. 3, the algorithm starts by acquiring the system data and applying per unit conversions. Then, the admittance matrices are constructed and factorized, and the load sequence component currents/powers are calculated. Consequently, the sequence component voltages and system frequency are solved for. The load flow variables are then updated and the phase node voltages are calculated. To take the DGs' capacity limits into account, the output powers of all DGs are evaluated at each iteration. If a DG exceeds its power limit, the output power is fixed at the maximum value, and the DG no longer follows the droop characteristics. The iteration is repeated until the results converge. It is worth noting that the loads, sequence load currents, decoupling components, and admittance matrices are updated at each iteration, as the microgrid's voltage magnitude and frequency change. The remainder of this section demonstrates the subroutines in the proposed algorithm.

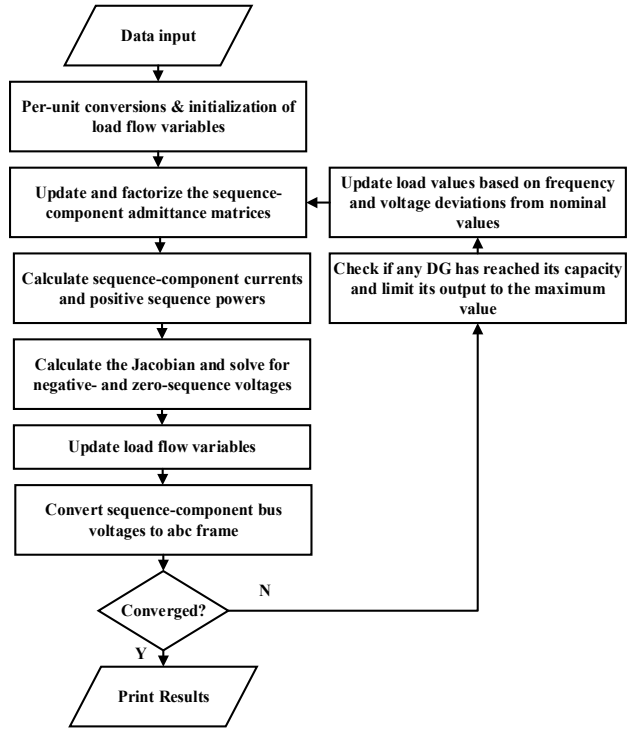

Fig. 3. Flow chart of the proposed power-flow algorithm

A. Positive-Sequence Power-Flow

Decoupling sequence-component circuits allows independent, yet correlated, solutions of the three subsystems. The positive sequence power-flow problem can be solved using the well-known NR method with some modifications. For a microgrid comprising N buses, $2N$ positive-sequence mismatch equations are defined for active and reactive powers at all buses. Assuming that all nodes integrate a DG and a load, generic active and reactive power mismatch equations can be formulated at an arbitrary bus *i* as

$$\Delta\mathcal{P}_i^1 = P_{G,i}^1 - P_{L,i}^1 - P_i^1 - \sum_{j\in\{N\setminus i\}} \Delta P_{i\_j}^1 \tag{31}$$

$$\Delta Q_i^1 = Q_{G,i}^1 - Q_{L,i}^1 - Q_i^1 - \sum_{j\in\{N\setminus i\}} \Delta Q_{i\_j}^1 \tag{32}$$

where P_i^1 and Q_i^1 are the active and reactive power injections at the bus *i*, which are defined by

This article has been accepted for publication in a future issue of this journal, but has not been fully edited. Content may change prior to final publication. Citation information: DOI 10.1109/TPWRS.2018.2820059, IEEE Transactions on Power Systems

$$P_i^1 = \sum_{j\in N} |V_i^1||V_j^1|\, Y_{ij}^{11}\, cos(\delta_i^1 - \delta_j^1 - \theta_{ij}^{11}) \tag{33}$$

$$Q_i^1 = \sum_{j\in N} |V_i^1||V_j^1|\, Y_{ij}^{11}\, sin(\delta_i^1 - \delta_j^1 - \theta_{ij}^{11}) \tag{34}$$

In (33) and (34), $|V_i^1|$ and $|V_j^1|$, and δ_i^1 and δ_j^1 are the positive-sequence voltage magnitudes and angles at nodes i and j, respectively, and Y_{ij}^{11} and θ_{ij}^{11} are the magnitude and angle of the positive-sequence Y-bus matrix element, respectively. Note that the absence of generation and/or load at a bus translates to substituting their powers with zeros. Considering that the microgrid frequency is primarily dependent on the positive-sequence power-flow, and by choosing the first bus's angle as a reference (i.e., $\delta_1^1 = 0$), $2N$ unknowns have to be solved for: N node voltages, the microgrid's frequency ω, and $N-1$ node angles. Thus, the positive-sequence voltage magnitudes, angles, and frequency for iteration $(k+1)$ in terms of the variables of iteration (k) are obtained as

$$\begin{bmatrix} |\boldsymbol{V^1}|_{(k+1)} \\ \omega_{(k+1)} \\ \boldsymbol{\delta^1_{(k+1)}} \end{bmatrix}_{2N\times 1} = \begin{bmatrix} |\boldsymbol{V^1}|_{(k)} \\ \omega_{(k)} \\ \boldsymbol{\delta^1_{(k)}} \end{bmatrix}_{2N\times 1} - [\,J\,]^{-1}_{(k)} \begin{bmatrix} \Delta\boldsymbol{\mathcal{P}}^1_{(k)} \\ \Delta\boldsymbol{Q}^1_{(k)} \end{bmatrix}_{2N\times 1} \tag{35}$$

where the Jacobian matrix J is formed as

$$[\,J\,] = \begin{bmatrix} \frac{\partial\Delta\boldsymbol{\mathcal{P}}^1}{\partial V^1} & \frac{\partial\Delta\boldsymbol{\mathcal{P}}^1}{\partial\omega} & \frac{\partial\Delta\boldsymbol{\mathcal{P}}^1}{\partial\delta^1} \\ \frac{\partial\Delta\boldsymbol{Q}^1}{\partial V^1} & \frac{\partial\Delta\boldsymbol{Q}^1}{\partial\omega} & \frac{\partial\Delta\boldsymbol{Q}^1}{\partial\delta^1} \end{bmatrix}_{2N\times 2N} \tag{36}$$

Due to the microgrid's droop characteristics, the Jacobean matrix elements are not exactly the same as those of conventional systems. By substituting from (12), (16), (17), (24), (25), (33), and (34) into (31) and (32), the matrix elements are obtained as (37)-(42). It is worth mentioning that for the derivatives with respect to the microgrid's frequency, the admittance is assumed constant, as its change has insignificant contribution to the Jacobian elements' values. However, the admittance variation is considered when calculating the mismatch equations to ensure accurate results.

$$\frac{\partial\Delta\mathcal{P}_i^1}{\partial\omega} \approx -\frac{\eta_i}{3} - P_{L,i}^1\, |V_i^1|^{\overline{\alpha_i}}\, \overline{K_{pf,\iota}} \tag{39}$$

$$\frac{\partial\Delta Q_i^1}{\partial\omega} \approx -Q_{L,i}^1\, |V_i^1|^{\overline{\beta_i}}\, \overline{K_{qf,\iota}} \tag{40}$$

$$\begin{cases} \dfrac{\partial\Delta\mathcal{P}_i^1}{\partial\delta_i^1} = |V_i^1| \displaystyle\sum_{j\in\{N\setminus i\}} |V_j^1|\, Y_{ij}^{11}\, sin(\delta_i^1 - \delta_j^1 - \theta_{ij}^{11}) \\ \dfrac{\partial\Delta\mathcal{P}_i^1}{\partial\delta_j^1} = -|V_i^1||V_j^1| Y_{ij}^{11}\, sin(\delta_i^1 - \delta_j^1 - \theta_{ij}^{11}) \end{cases} \tag{41}$$

$$\begin{cases} \dfrac{\partial\Delta Q_i^1}{\partial\delta_i^1} = -|V_i^1| \displaystyle\sum_{j\in\{N\setminus i\}} |V_j^1|\, Y_{ij}^{11}\, cos(\delta_i^1 - \delta_j^1 - \theta_{ij}^{11}) \\ \dfrac{\partial\Delta Q_i^1}{\partial\delta_j^1} = |V_i^1||V_j^1| Y_{ij}^{11}\, cos(\delta_i^1 - \delta_j^1 - \theta_{ij}^{11}) \end{cases} \tag{42}$$

Bars above load parameters (i.e., α, β, K_{pf}, and K_{qf}) in (26)-(29) denote their averaged values over the unbalanced loads at node i.

B. Negative- and Zero-Sequence Power-Flows

The negative and zero sequence voltages for the same iteration $(k+1)$ can be directly calculated by solving

$$\boldsymbol{V^2_{(k+1)}} = \left[Y^{22}_{(k+1)}\right]^{-1}_{N\times N}\left[-\boldsymbol{I^2_{L\,(k+1)}} - \Delta\boldsymbol{I^2_{(k+1)}}\right]_{N\times 1} \tag{43}$$

$$\boldsymbol{V^0_{(k+1)}} = \left[Y^{00}_{(k+1)}\right]^{-1}_{N\times N}\left[-\boldsymbol{I^0_{L\,(k+1)}} - \Delta\boldsymbol{I^0_{(k+1)}}\right]_{N\times 1} \tag{44}$$

where the decoupling current vectors ΔI^2 and ΔI^0 are constructed by calculating the total decoupling currents at each bus i as

$$\Delta I_i^2 = \sum_{j\in\{N\setminus i\}} \Delta I_{i\_j}^2 \tag{45}$$

$$\Delta I_i^0 = \sum_{j\in\{N\setminus i\}} \Delta I_{i\_j}^0 \tag{46}$$

Furthermore, since equations (31) and (32) assume three-phase feeders and Y-connected loads, all delta-connected loads must be pre-processed using (29) and (30) at each iteration.

C. Comparison with the Problem Formulation of the NTR method

The NTR-based approach, reported in [12], formulates the unbalanced power-flow problem in phase coordinates. Accordingly, the power-flow problem comprises 6 equations at each node to represent the active and reactive power mismatches for the three phases, leading to a problem size of $(6N \times 6N)$. Furthermore, the adopted NTR solution method is formulated as an optimization algorithm to minimize the mismatch powers (ideally to zero). Although this method demonstrates good convergence performance in terms of robustness and number of iterations, its computational cost is significantly high due to the problem's large size. On the other hand, as per (35), (43) and (44), the proposed approach breaks the power-flow problem down into three independent sub-problems of sizes $(2N \times 2N)$, $(N \times N)$, and $(N \times N)$, for the decoupled positive-, negative-, and zero-sequence subsystems, respectively. Such reduction in problem size results in substantial decrease in computational and memory requirements of the problem solution, even when including the decoupling computational overhead in the proposed method [23]. Meanwhile, the proposed approach allows parallel solution of the sub-problems, which leads to further reduction in the algorithm's execution time. Additionally, the NTR method evaluates the gradient and Hessian matrices numerically, thus adding considerable computational burden to the algorithm; this burden significantly escalates as the microgrid size increases. On the

$$\begin{cases} \dfrac{\partial\Delta\mathcal{P}_i^1}{\partial V_i^1} = -\overline{\alpha_i} P_{L,i}^1 |V_i^1|^{\overline{\alpha_i}-1}\left(1 + \overline{K_{pf,\iota}}\,\Delta\omega\right) - 2|V_i^1|\, Y_{ii}^{11}\, cos(\theta_{ii}^{11}) - \displaystyle\sum_{j\in\{N\setminus i\}} |V_j^1|\, Y_{ij}^{11}\, cos(\delta_i^1 - \delta_j^1 - \theta_{ij}^{11}) \\ \dfrac{\partial\Delta\mathcal{P}_i^1}{\partial V_j^1} = -|V_i^1| Y_{ij}^{11}\, cos(\delta_i^1 - \delta_j^1 - \theta_{ij}^{11}) \end{cases} \tag{37}$$

$$\begin{cases} \dfrac{\partial\Delta Q_i^1}{\partial V_i^1} = -\dfrac{\mu_i}{3} - \overline{\beta_i} Q_{L,i}^1 |V_i^1|^{\overline{\beta_i}-1}\left(1 + \overline{K_{qf,\iota}}\,\Delta\omega\right) + 2|V_i^1|\, Y_{ii}^{11}\, sin(\theta_{ii}^{11}) - \displaystyle\sum_{j\in\{N\setminus i\}} |V_j^1| Y_{ij}^{11}\, sin(\delta_i^1 - \delta_j^1 - \theta_{ij}^{11}) \\ \dfrac{\partial\Delta Q_i^1}{\partial V_j^1} = -|V_i^1|\, Y_{ij}^{11}\, sin(\delta_i^1 - \delta_j^1 - \theta_{ij}^{11}) \end{cases} \tag{38}$$

This article has been accepted for publication in a future issue of this journal, but has not been fully edited. Content may change prior to final publication. Citation information: DOI 10.1109/TPWRS.2018.2820059, IEEE Transactions on Power Systems

contrary, the Jacobian matrix elements are directly calculated through (37)-(42) in the proposed approach, thereby resulting in minimal computational effort. Altogether, these factors give remarkable advantage to the proposed approach's performance over that of its NTR-based counterpart.

V. Performance Validation of the Proposed Approach

The performance of the proposed modeling and power-flow algorithm was validated through comparison of accuracy and computational time against time-domain simulations and a traditional NTR-based algorithm.

A. Comparison with time-domain simulations

The power-flow algorithm was tested on a modified IEEE 13-node test feeder [13], shown in Fig. 4. Three droop-controlled DGs of different types, sizes, and settings, presented in Table I, were connected to buses 650, 681, and 692. The SGDG's ratings and parameters can be found in [24]. Furthermore, a 2.5 MVA delta-wye transformer interfaces the 3-leg EIDG to the 4-wire network; its short-circuit resistance and reactance at 60 Hz are 1% and 6%, respectively. Although the system is relatively small, it includes all different components of distribution systems, namely, untransposed feeders, unbalanced loads, different load connections, distribution transformers, and single- and two-phase laterals and loads. The microgrid's small size allows conducting detailed time-domain simulations for model validation.

A complete time-domain model of the test microgrid was constructed and run in MATLAB/Simulink environment until it converged to a steady state. The proposed algorithm, implemented in MATLAB, was also executed to solve the same power-flow problem. Table II shows close agreement between the power-flow results obtained based on the proposed models and solution algorithm and those of the time-domain simulations. The mismatches are smaller than 6.06×10^{-4} pu, $0.13°$ (2.36×10^{-3} rad), and 5.72×10^{-5} pu for the voltage magnitude, angle, and frequency, respectively, validating the accuracy of the proposed method.

B. Robustness of the Proposed Approach

It is important to ensure that a power-flow algorithm is robust and able to converge under various conditions. Therefore, the robustness of the proposed approach was examined under light and heavy microgrid loading conditions, which may result in over- and under-voltages, respectively. The loads of test microgrid#1 were multiplied by a factor λ to change the microgrid loading, as per

$$P_{L,i}^{0,x} + jQ_{L,i}^{0,x} = \lambda\,(P_{L,i\_base}^{0,x} + j\,Q_{L,i\_base}^{0,x}) \quad (47)$$

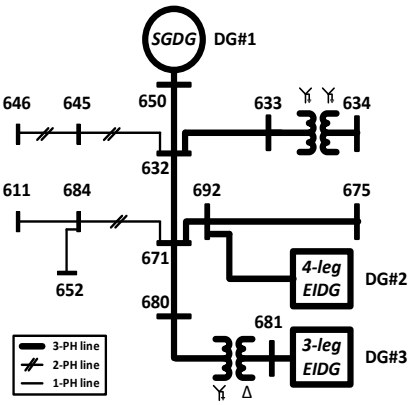

Fig. 4. Test microgrid#1: modified IEEE 13-node test feeder

TABLE I
DG Ratings and Droop Settings

DG#	DG Type	η (pu)	μ (pu)	ω_0 (pu)	V_0 (pu)	P_G^{max} (pu)	S_G^{max} (pu)
1	SGDG	25.2	7.56	1.00	1.00	0.504	0.630
2	4-leg EIDG	18.0	5.40	1.00	1.00	0.360	0.450
3	3-leg EIDG	20.0	6.00	1.00	1.00	0.400	0.500

Table III shows the maximum and minimum observed voltages of the microgrid under each loading condition. Furthermore, for a power mismatch tolerance of 1.0×10^{-6}, the table shows the number of iterations for convergence in each case. The results demonstrate that for the no-load condition (i.e., $\lambda = 0$), the connected capacitors boost the microgrid voltage above the DG's set points. They also result in unbalanced microgrid operation. On the contrary, heavy loading condition (i.e., $\lambda = 1.5$) results in under-voltages at some microgrid nodes. In all cases, the proposed algorithm converges in 7 or 8 iterations, proving the proposed approach robust under different loading and voltage conditions.

C. Performance Comparison with the NTR-based approach

To further validate the accuracy and performance of the proposed approach, a performance comparison against the NTR method was performed through solving the power-flow of the 25-node microgrid in [12], which considered the integration of three identical droop-controlled DGs. Both algorithms were executed on a PC with a 64-bit Intel Core i7 @3.4 GHz CPU and 16 GB of RAM. The two methods were initialized at a three-phase flat start: the NTR method adopted a flat start in phase coordinates (i.e., all nodes were assigned $V_a = 1.0\angle 0.0°$ p.u., $V_b = 1.0\angle -120.0°$ p.u., and $V_c = 1.0\angle 120.0°$ p.u.), while the proposed method was initialized in symmetrical sequence components (i.e., all nodes were assigned $V^0 = 0.0$ p.u., $V^1 = 1.0\angle 0.0°$ p.u., and $V^2 = 0.0$ p.u.). The microgrid's frequency was assumed to be initially 1.0

TABLE II
Power-Flow Results of Test Microgrid #1

	MATLAB/Simulink (ω = 0.98951 pu)			Proposed Method (ω = 0.98957 pu)		
Bus#	V_a (pu)	V_b (pu)	V_c (pu)	V_a (pu)	V_b (pu)	V_c (pu)
650	**0.9921 ∠ 0.00**	**0.9845 ∠ −120.30**	**0.9863 ∠ 120.13**	**0.9920 ∠ 0.00**	**0.9839 ∠ −120.25**	**0.9866 ∠ 120.19**
632	0.9802 ∠ − 0.65	0.9709 ∠ − 121.43	0.9765 ∠ 119.08	0.9803 ∠ − 0.57	0.9709 ∠ − 121.34	0.9765 ∠ 119.17
633	0.9772 ∠ − 0.72	0.9691 ∠ − 121.48	0.9740 ∠ 119.08	0.9774 ∠ − 0.63	0.9690 ∠ − 121.38	0.9740 ∠ 119.16
634	0.9546 ∠ − 1.38	0.9514 ∠ − 121.95	0.9561 ∠ 118.60	0.9548 ∠ − 1.29	0.9513 ∠ − 121.85	0.9562 ∠ 118.70
645		0.9620 ∠ − 121.62	0.9747 ∠ 119.10		0.9620 ∠ − 121.52	0.9747 ∠ 119.19
646		0.9604 ∠ − 121.55	0.9727 ∠ 119.15		0.9604 ∠ − 121.60	0.9728 ∠ 119.24
671	0.9760 ∠ − 1.43	0.9759 ∠ − 121.41	0.9763 ∠ 118.58	0.9762 ∠ − 1.30	0.9762 ∠ − 121.30	0.9762 ∠ 118.70
680	0.9804 ∠ − 1.06	0.9791 ∠ − 121.01	0.9804 ∠ 118.98	0.9804 ∠ − 0.96	0.9791 ∠ − 120.92	0.9803 ∠ 119.09
681	**0.9906 ∠ − 29.62**	**0.9906 ∠ − 149.63**	**0.9906 ∠ 90.37**	**0.9906 ∠ − 29.54**	**0.9906 ∠ − 149.54**	**0.9906 ∠ 90.46**
684	0.9740 ∠ − 1.46		0.9743 ∠ 118.48	0.9742 ∠ − 1.32		0.9742 ∠ 118.60
611			0.9724 ∠ 118.34			0.9723 ∠ 118.46
652	0.9685 ∠ − 1.38			0.9688 ∠ − 1.25		
692	**0.9760 ∠ − 1.43**	**0.9759 ∠ − 121.41**	**0.9763 ∠ 118.58**	**0.9762 ∠ − 1.30**	**0.9762 ∠ − 121.30**	**0.9762 ∠ 118.70**
675	0.9700 ∠ − 1.67	0.9781 ∠ − 121.58	0.9742 ∠ 118.60	0.9701 ∠ − 1.54	0.9783 ∠ − 121.47	0.9743 ∠ 118.70

This article has been accepted for publication in a future issue of this journal, but has not been fully edited. Content may change prior to final publication. Citation information: DOI 10.1109/TPWRS.2018.2820059, IEEE Transactions on Power Systems

TABLE III
ROBUSTNESS RESULTS (TEST MICROGRID#1)

λ	0	0.5	1	1.5
Max node voltage	1.0143	0.9990	0.9920	0.9852
Min node voltage	1.0054	0.9793	0.9513	0.9246
#iterations	8	7	8	8

TABLE IV
PERFORMANCE COMPARISON (25-NODE MICROGRID [12])

	Proposed Method		NTR [12]	
Tolerance	1.0×10^{-6}	1.0×10^{-12}	1.0×10^{-6}	1.0×10^{-12}
Solution time (ms)	75	108	3,220	3,893
# iterations	3	7	3	4

p.u for both methods. The stopping criterion was unified and selected such that the gradient norm did not exceed the specified tolerance value. The two approaches produce similar results if directly-connected 4-leg EIDGs are assumed in the proposed method. However, the NTR-based approach fails to produce accurate results when the transformers' effects and/or other types of DGs are considered. The reason for this inaccuracy is neglecting the interfacing transformers' effects and assuming that all DG types can maintain balanced terminal voltages. Furthermore, the proposed algorithm demonstrates considerably improved solution time, as shown in Table IV, for two tolerance values. The results prove that the proposed approach outperforms its NTR-based counterpart not only in accuracy, but also in efficiency.

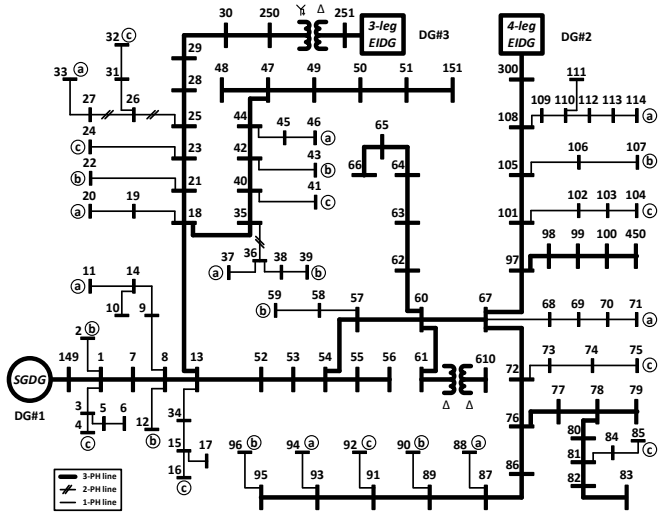

Fig. 5. Test microgrid#2: modified IEEE 123-node test feeder

VI. CASE STUDIES

The following case studies highlight the effectiveness of the proposed algorithm in solving larger and more complex microgrids. The modified IEEE 123-node test feeder has been adopted to form a test microgrid by adding three DG units to nodes 149, 251, and 300, as shown in Fig. 5. While the system structure remained the same, the two microgrid operational control modes

TABLE V
POWER-FLOW RESULTS OF TEST MICROGRID#2

Bus#	V_a (pu)	V_b (pu)	V_c (pu)	Bus#	V_a (pu)	V_b (pu)	V_c (pu)	Bus#	V_a (pu)	V_b (pu)	V_c (pu)
149	**0.9815 ∠ 0.00**	**0.9861 ∠ –119.49**	**0.9868 ∠ 120.17**	38		0.9752 ∠ –120.04		77	0.9695 ∠ –1.60	0.9747 ∠ –121.05	0.9738 ∠ 118.75
1	0.9770 ∠ –0.25	0.9846 ∠ –119.63	0.9826 ∠ 120.02	39		0.9748 ∠ –120.05		78	0.9698 ∠ –1.62	0.9751 ∠ –121.06	0.9739 ∠ 118.73
2		0.9844 ∠ –119.63		40	0.9618 ∠ –0.76	0.9752 ∠ –120.03	0.9725 ∠ 119.86	79	0.9695 ∠ –1.63	0.9752 ∠ –121.07	0.9739 ∠ 118.74
3			0.9809 ∠ 119.99	41			0.9721 ∠ 119.85	80	0.9717 ∠ –1.68	0.9766 ∠ –121.12	0.9746 ∠ 118.62
4			0.9804 ∠ 119.98	42	0.9603 ∠ –0.80	0.9741 ∠ –120.08	0.9716 ∠ 119.82	81	0.9737 ∠ –1.76	0.9787 ∠ –121.15	0.9750 ∠ 118.51
5			0.9797 ∠ 119.97	43		0.9729 ∠ –120.10		82	0.9745 ∠ –1.80	0.9799 ∠ –121.18	0.9757 ∠ 118.48
6			0.9790 ∠ 119.96	44	0.9592 ∠ –0.83	0.9734 ∠ –120.11	0.9708 ∠ 119.79	83	0.9756 ∠ –1.82	0.9809 ∠ –121.21	0.9765 ∠ 118.43
7	0.9736 ∠ –0.42	0.9836 ∠ –119.74	0.9803 ∠ 119.95	45	0.9586 ∠ –0.84			84			0.9723 ∠ 118.46
8	0.9715 ∠ –0.53	0.9828 ∠ –119.82	0.9788 ∠ 119.90	46	0.9582 ∠ –0.85			85			0.9710 ∠ 118.43
9	0.9700 ∠ –0.56			47	0.9582 ∠ –0.85	0.9724 ∠ –120.14	0.9698 ∠ 119.74	86	0.9674 ∠ –1.57	0.9718 ∠ –121.14	0.9744 ∠ 118.80
10	0.9681 ∠ –0.60			48	0.9579 ∠ –0.86	0.9721 ∠ –120.15	0.9696 ∠ 119.74	87	0.9668 ∠ –1.59	0.9710 ∠ –121.24	0.9749 ∠ 118.78
11	0.9678 ∠ –0.60			49	0.9579 ∠ –0.86	0.9718 ∠ –120.15	0.9695 ∠ 119.72	88	0.9667 ∠ –1.62		
12		0.9825 ∠ –119.83		50	0.9579 ∠ –0.87	0.9718 ∠ –120.14	0.9691 ∠ 119.71	89	0.9664 ∠ –1.59	0.9707 ∠ –121.28	0.9753 ∠ 118.76
13	0.9694 ∠ –0.65	0.9813 ∠ –119.92	0.9765 ∠ 119.80	51	0.9577 ∠ –0.88	0.9719 ∠ –120.14	0.9691 ∠ 119.71	90		0.9706 ∠ –121.32	
14	0.9684 ∠ –0.59			52	0.9676 ∠ –0.82	0.9804 ∠ –120.09	0.9757 ∠ 119.65	91	0.9662 ∠ –1.59	0.9704 ∠ –121.30	0.9754 ∠ 118.75
15			0.9751 ∠ 119.77	53	0.9670 ∠ –0.89	0.9799 ∠ –120.18	0.9753 ∠ 119.57	92			0.9753 ∠ 118.69
16			0.9741 ∠ 119.75	54	0.9668 ∠ –0.93	0.9794 ∠ –120.23	0.9751 ∠ 119.52	93	0.9658 ∠ –1.59	0.9702 ∠ –121.32	0.9755 ∠ 118.75
17			0.9746 ∠ 119.76	55	0.9666 ∠ –0.93	0.9793 ∠ –120.24	0.9752 ∠ 119.52	94	0.9651 ∠ –1.61		
18	0.9661 ∠ –0.63	0.9789 ∠ –119.89	0.9746 ∠ 119.97	56	0.9665 ∠ –0.93	0.9791 ∠ –120.25	0.9752 ∠ 119.52	95	0.9658 ∠ –1.58	0.9698 ∠ –121.34	0.9757 ∠ 118.75
19	0.9648 ∠ –0.66			57	0.9669 ∠ –1.04	0.9778 ∠ –120.38	0.9745 ∠ 119.38	96		0.9695 ∠ –121.34	
20	0.9639 ∠ –0.68			58		0.9771 ∠ –120.39		97	0.9697 ∠ –1.29	0.9759 ∠ –120.74	0.9735 ∠ 119.05
21	0.9676 ∠ –0.52	0.9795 ∠ –119.79	0.9755 ∠ 120.04	59		0.9768 ∠ –120.40		98	0.9694 ∠ –1.30	0.9757 ∠ –120.75	0.9734 ∠ 119.04
22		0.9782 ∠ –119.82		60	0.9674 ∠ –1.29	0.9754 ∠ –120.65	0.9727 ∠ 119.09	99	0.9697 ∠ –1.29	0.9748 ∠ –120.76	0.9731 ∠ 119.00
23	0.9689 ∠ –0.44	0.9804 ∠ –119.69	0.9761 ∠ 120.10	61	0.9674 ∠ –1.29	0.9754 ∠ –120.65	0.9727 ∠ 119.09	100	0.9699 ∠ –1.29	0.9748 ∠ –120.75	0.9727 ∠ 118.98
24			0.9746 ∠ 120.07	610	0.9674 ∠ –1.29	0.9754 ∠ –120.65	0.9727 ∠ 119.09	450	0.9699 ∠ –1.29	0.9748 ∠ –120.75	0.9727 ∠ 118.98
25	0.9701 ∠ –0.35	0.9814 ∠ –119.59	0.9771 ∠ 120.18	62	0.9666 ∠ –1.29	0.9743 ∠ –120.63	0.9706 ∠ 119.08	101	0.9713 ∠ –1.20	0.9767 ∠ –120.71	0.9744 ∠ 119.09
26	0.9699 ∠ –0.37		0.9766 ∠ 120.16	63	0.9660 ∠ –1.28	0.9734 ∠ –120.61	0.9696 ∠ 119.07	102			0.9729 ∠ 119.06
27	0.9695 ∠ –0.39		0.9766 ∠ 120.16	64	0.9657 ∠ –1.26	0.9716 ∠ –120.58	0.9674 ∠ 119.04	103			0.9714 ∠ 119.03
28	0.9711 ∠ –0.27	0.9820 ∠ –119.52	0.9781 ∠ 120.25	65	0.9651 ∠ –1.27	0.9713 ∠ –120.53	0.9644 ∠ 119.03	104			0.9695 ∠ 118.99
29	0.9730 ∠ –0.12	0.9827 ∠ –119.41	0.9798 ∠ 120.33	66	0.9653 ∠ –1.29	0.9715 ∠ –120.50	0.9629 ∠ 119.03	105	0.9726 ∠ –1.10	0.9776 ∠ –120.71	0.9763 ∠ 119.18
30	0.9757 ∠ 0.06	0.9834 ∠ –119.29	0.9817 ∠ 120.41	67	0.9683 ∠ –1.37	0.9754 ∠ –120.76	0.9728 ∠ 119.01	106		0.9764 ∠ –120.73	
250	0.9770 ∠ 0.17	0.9838 ∠ –119.22	0.9831 ∠ 120.47	68	0.9667 ∠ –1.40			107		0.9749 ∠ –120.76	
251	**0.9915 ∠ –28.05**	**0.9915 ∠ –148.05**	**0.9915 ∠ 91.95**	69	0.9648 ∠ –1.44			108	0.9742 ∠ –1.00	0.9797 ∠ –120.66	0.9780 ∠ 119.30
31			0.9760 ∠ 120.15	70	0.9635 ∠ –1.47			**300**	**0.9838 ∠ –0.47**	**0.9838 ∠ –120.47**	**0.9838 ∠ 119.53**
32			0.9756 ∠ 120.14	71	0.9627 ∠ –1.48			109	0.9700 ∠ –1.08		
33	0.9682 ∠ –0.42			72	0.9686 ∠ –1.47	0.9744 ∠ –120.87	0.9725 ∠ 118.88	110	0.9680 ∠ –1.12		
34			0.9755 ∠ 119.78	73			0.9703 ∠ 118.84	111	0.9673 ∠ –1.14		
35	0.9633 ∠ –0.72	0.9764 ∠ –119.98	0.9735 ∠ 119.91	74			0.9685 ∠ 118.80	112	0.9674 ∠ –1.13		
36	0.9624 ∠ –0.74	0.9759 ∠ –120.03		75			0.9674 ∠ 118.78	113	0.9654 ∠ –1.17		
37	0.9617 ∠ –0.75			76	0.9684 ∠ –1.53	0.9737 ∠ –120.97	0.9731 ∠ 118.83	114	0.9649 ∠ –1.18		

This article has been accepted for publication in a future issue of this journal, but has not been fully edited. Content may change prior to final publication. Citation information: DOI 10.1109/TPWRS.2018.2820059, IEEE Transactions on Power Systems

TABLE VI
DG OUTPUT PHASE POWERS FOR TEST MICROGRID#2

DG#	Node#	P_a (pu)	P_b (pu)	P_c (pu)	Q_a (pu)	Q_b (pu)	Q_c (pu)
1	149	0.1042	0.0817	0.0902	0.0390	0.0310	0.0448
2	300	0.0855	0.0467	0.0649	0.0425	0.0243	0.0207
3	250	0.0883	0.0576	0.0721	0.0235	0.0110	0.0101
3	251	0.0849	0.0692	0.0650	0.0146	0.0284	0.0079

TABLE VII
ROBUSTNESS RESULTS (TEST MICROGRID#2)

λ	0	0.5	1	1.5
Max node voltage	1.0284	1.0048	0.9915	0.9844
Min node voltage	1.0046	0.9840	0.9577	0.9308
#iterations	8	7	7	7

TABLE VIII
PERFORMANCE COMPARISON (TEST MICROGRID#2)

	Proposed Method		NTR [12]	
Tolerance	1.0×10^{-6}	1.0×10^{-12}	1.0×10^{-6}	1.0×10^{-12}
Solution time (ms)	467	1,009	111,849	144,827
# iterations	3	10	3	4

(i.e., droop and isochronous) are investigated in the two following subsections.

A. Droop-Controlled Microgrid

In this analysis, the DGs implement droop characteristics according to the parameters stated in Table I. The voltage magnitudes and angles of all buses are presented in Table V and the DGs collaboratively set the steady-state frequency ω to 0.98905 pu. The results demonstrate three key aspects pertaining to the behaviors of different types of DGs under unbalanced operation. First, while the 4-leg EIDG with negative- and zero-sequence voltage compensation maintains balanced voltages at its terminals (node#300), the 3-wire EIDG cannot compensate for zero-sequence voltages behind the interfacing transformers, as observed at node#250. Second, the SGDG encounters unbalanced terminal voltages (node#149) due to its internal impedances. Third, the effect of the transformer delta-wye connection on the DG phase loading can be concluded from the results in Table VI. It is observed that not only the total DG active and reactive powers are higher at the DG terminals (node#251) than those at the microgrid's bus (node#250) due to the transformer impedance, but also the power unbalances among the three phases are different at the two nodes because of the transformer delta/wye connection. This analysis is critical, in particular, for microgrids' loadability studies [25], [26]. The proposed method accounts for various system components and their different characteristics, which ensures more accurate analysis compared to other methods.

To further investigate the robustness and performance of the proposed approach in solving large-scale microgrids, the analysis performed in subsections V.B and V.C were repeated for test microgrid#2. Table VII presents the maximum and minimum microgrid voltages as well as the number of iterations for the algorithm to converge. Meanwhile, Table VIII compares the proposed approach's performance against that of the NTR method. It is noteworthy that since the NTR approach does not model delta-connected loads, the microgrid loads were all converted to wye-connection, for the sake of performance comparison. As seen in Table VIII, the performance superiority of the proposed algorithm, in comparison with the NTR algorithm, becomes more evident with the increase in the microgrid size. Overall, the results solidify the previously obtained ones for test microgrid#1, and therefore they confirm the approach's robustness and enhanced performance over the conventional one.

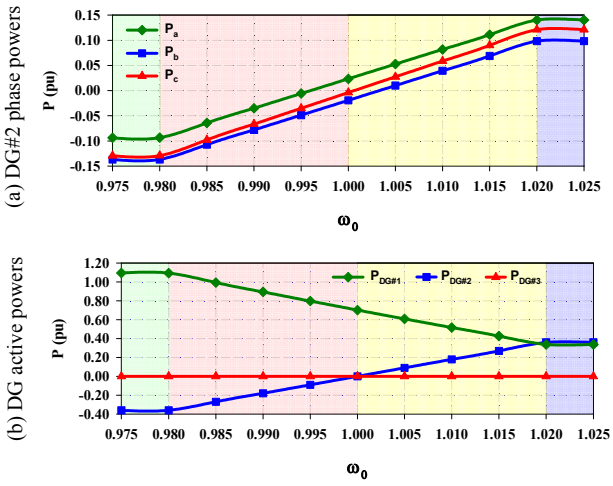

Fig. 6. Effects of changing the droop frequency set-point on active powers

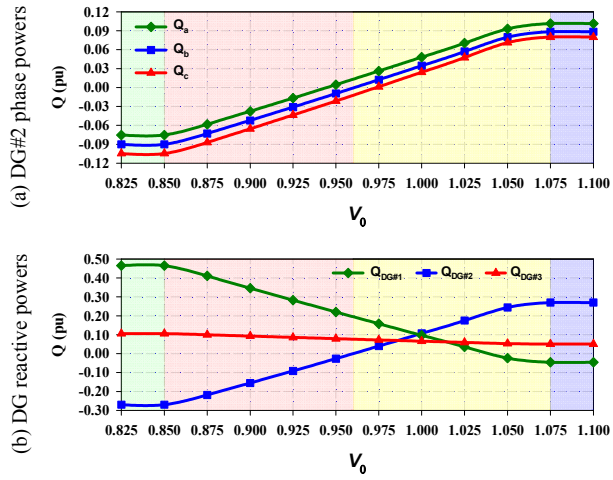

Fig. 7. Effects of changing the droop voltage set-point on reactive powers

B. Isochronously-Controlled Microgrid

This case studies the microgrid's isochronous operation. The active and reactive power ratings of SGDG (DG#1) are increased to 4.0 and 5.0 pu, respectively, allowing it to dominate the microgrid's operation. Furthermore, its droop gains η and μ are set to infinity, resulting in tight regulation of microgrid's frequency at its reference value of $\omega_0 = 1.00$ pu. On the other hand, DG#2 and DG#3 are droop-controlled and their droop set-points, ω_0 and V_0, can be adjusted to control their output powers.

To examine the effect of changing the frequency set-point on the microgrid operation, DG#2's frequency set-point ω_0 was gradually changed from 0.975 to 1.025 pu, while DG#3's was kept constant at 1.00 pu. Fig. 6 (a) depicts the change of the output active power of the three phases of DG#2, while Fig 6 (b) shows the total output power of the three DGs. Although the output power of the three-phases are unequal due to the system unbalances, it can generally be observed that the phase active powers proportionally increase with the frequency set-point if set above the microgrid frequency (i.e., $\omega_0 > 1.00$ pu). Furthermore, as the set-point is decreased below the microgrid frequency (i.e., $\omega_0 < 1.00$ pu), the active power reverses direction meaning that the DG absorbs power, which can be desirable for ESSs. Moreover, as DG#2 approaches its active power capacity in either direction (i.e., $\omega_0 < 0.98$ pu or $\omega_0 > 1.02$ pu), the power is limited to the maximum value, which verifies the effectiveness of the proposed algorithm in enforcing DG limits in the solution. Note that, as illustrated in Fig. 6 (b), the

total output active power of DG#3 is zero regardless of the set-point of DG#2 because its set-point is fixed at the microgrid's frequency. However, as DG#2's active power changes, the isochronous DG autonomously adjusts its power to maintain successful microgrid operation, since it acts as a non-ideal slack bus.

Similarly, DG#2's voltage set-point V_0 was gradually changed from 0.825 to 1.100 pu. The corresponding phase reactive powers are plotted in Fig. 7 (a). Unlike the microgrid frequency, the voltage is not a global variable, and thus the DG injects reactive power at $V_0 = 1.00$ pu due to voltage drops across the feeders. Nevertheless, the DG's reactive power approaches zero at $V_0 \approx 0.96$ pu where the set-point is almost equal to the DG's positive-sequence terminal voltage. Below this value, DG#2 absorbs reactive power from the microgrid. The algorithm is also capable of limiting the DG's reactive power as it approaches its maximum value in either direction. The effect of changing DG#2's voltage set-point on other DGs is demonstrated in Fig. 7 (b). The figure shows that, due to different deviations in bus voltages, DG#3's reactive power is neither zero nor constant as DG#2's voltage set-point is being changed. However, the significant reactive power changes are observed in the controlled DG (i.e., DG#2) and the isochronous SGDG, as it maintains the reactive power balance of the microgrid.

It is worth mentioning that the results also illustrate the algorithm's robustness when solving isochronous microgrids, as it converged under a wide range of DG settings. Although the microgrid's node voltages varied from values as low as 0.9016 p.u. at $V_0 = 0.825$ p.u. to values as high as 1.0093 p.u. at $V_0 = 1.10$ p.u., the algorithm successfully converged under both normal and extreme operating conditions.

VII. Conclusion

Steady-state analysis is crucial for planning and operation studies of microgrids. Since microgrids can be controlled in either droop or isochronous modes, the development of a generic, accurate, and efficient power-flow analysis approach becomes essential. The unbalanced nature of distribution networks and the possibility of the coexistence of SGDGs and EIDGs entails precise modeling of their different characteristics. In this work, a generalized methodology based on symmetrical sequence component analysis of microgrids was developed. The models of different DG types were presented and integrated into the power-flow formulation. An NR algorithm was used to solve the power-flow problem while taking the DG droop characteristics and power limits into consideration.

The IEEE 13-node test feeder was modified to form a droop-controlled microgrid for model and algorithm validation. The detailed time-domain model of the test system was built and simulated in MATLAB/Simulink. The close match between the results of the algorithm and time-domain simulations proves the accuracy of the developed method. Furthermore, two case studies, incorporating a modified IEEE 123-node test microgrid, were introduced to examine the effectiveness of the proposed method in analyzing more complex microgrids, and to study the operation of droop-based DGs in isochronous microgrids. The results shed light on the use of droop settings for 4-quadrant control of dispatchable units in isochronous microgrids. They also show the effectiveness of the proposed algorithm in limiting the DGs' powers, in both directions, as they approach their limits.

Moreover, the robustness of the proposed algorithm was tested through changing the test microgrids' operational conditions from light to heavy loading, and from droop to isochronous modes of operation. The algorithm demonstrated rigid convergence characteristics under the various testing conditions. Furthermore, the algorithm showed superior performance in terms of accuracy and execution time, when compared to the reported NTR approach.

References

[1] D. E. Olivares *et al.*, "Trends in Microgrid Control," *IEEE Trans. Smart Grid*, vol. 5, no. 4, pp. 1905–1919, Jul. 2014.

[2] J. M. Guerrero, J. C. Vasquez, J. Matas, L. G. De Vicuña, and M. Castilla, "Hierarchical control of droop-controlled AC and DC microgrids - A general approach toward standardization," *IEEE Trans. Ind. Electron.*, vol. 58, no. 1, pp. 158–172, 2011.

[3] M. Arriaga, C. A. Canizares, and M. Kazerani, "Long-Term Renewable Energy Planning Model for Remote Communities," *IEEE Trans. Sustain. Energy*, vol. 7, no. 1, pp. 221–231, 2016.

[4] F. Katiraei, R. Iravani, N. Hatziargyriou, and A. Dimeas, "Microgrids Management: Controls and Operation Aspects of Microgrids," *IEEE Power & Energy Magazine*, no. June, pp. 54–65, 2008.

[5] Z. Miao, A. Domijan, and L. Fan, "Investigation of microgrids with both inverter interfaced and direct AC-connected distributed energy resources," *IEEE Trans. Power Del.*, vol. 26, no. 3, pp. 1634–1642, 2011.

[6] A. R. Bergen and V. Vittal, *Power Systems Analysis*, 2nd ed. New Jersey: Prentice Hall, 2000.

[7] M. Abdel-Akher, K. M. Nor, and A. H. A. Rashid, "Improved three-phase power-flow methods using sequence components," *IEEE Trans. Power Syst.*, vol. 20, no. 3, pp. 1389–1397, 2005.

[8] M. Z. Kamh and R. Iravani, "Unbalanced model and power-flow analysis of microgrids and active distribution systems," *IEEE Trans. Power Del.*, vol. 25, no. 4, pp. 2851–2858, 2010.

[9] F. Mumtaz, M. H. Syed, M. Al Hosani, and H. H. Zeineldin, "A Novel Approach to Solve Power Flow for Islanded Microgrids Using Modified Newton Raphson with Droop Control of DG," *IEEE Trans. Sustain. Energy*, vol. 7, no. 2, pp. 493–503, 2016.

[10] A. A. Hamad, M. A. Azzouz, and E. F. El Saadany, "A Sequential Power Flow Algorithm for Islanded Hybrid AC/DC Microgrids," *IEEE Trans. Power Syst.*, vol. 31, no. 5, pp. 3961–3970, 2016.

[11] M. E. Nassar and M. M. A. Salama, "A novel branch-based power flow algorithm for islanded AC microgrids," *Electric Power Systems Research*, vol. 146, pp. 51–62, 2017.

[12] M. M. A. Abdelaziz, H. E. Farag, E. F. El-Saadany, and Y. A. R. I. Mohamed, "A Novel and Generalized Three-Phase Power Flow Algorithm for Islanded Microgrids Using a Newton Trust Region Method," *IEEE Trans. Power Syst.*, vol. 28, no. 1, pp. 190–201, 2013.

[13] W. H. Kersting, "Radial distribution test feeders," in *2001 IEEE Power Engineering Society Winter Meeting. Conference Proceedings*, 2001, no. 2, pp. 908–912.

[14] J. Rocabert, A. Luna, F. Blaabjerg, and P. Rodriguez, "Control of power converters in AC microgrids," *IEEE Trans. Power Electron.*, vol. 27, no. 11, pp. 4734–4749, 2012.

[15] M. Arriaga, C. Cañizares, and M. Kazerani, "Renewable energy alternatives for remote communities in Northern Ontario, Canada," *IEEE Trans. Sustain. Energy*, vol. 4, no. 3, pp. 661–670, 2013.

[16] Y. S. Tamura J, Takeda I, Kimura M, UENO M, "A synchronous machine model for unbalanced analysis," *Elect. Eng. Jpn.*, vol. 119, no. 2, pp. 46–59, 1997.

[17] J. C. Vasquez, J. M. Guerrero, M. Savaghebi, J. Eloy-garcia, and R. Teodorescu, "Modeling , Analysis , and Design of Parallel Three-Phase Voltage Source Inverters," *IEEE Trans. Ind. Electron.*, vol. 60, no. 4, pp. 1271–1280, 2013.

[18] P. T. Cheng, C. A. Chen, T. L. Lee, and S. Y. Kuo, "A cooperative imbalance compensation method for distributed-generation interface converters," *IEEE Trans. Ind. Appl.*, vol. 45, no. 2, pp. 805–815, 2009.

[19] J. Arrillaga and N. R. Watson, *Computer modeling of electrical power systems*, 2nd ed. New York: Wiley, 2001.

[20] M. Z. Kamh and R. Iravani, "A unified three-phase power-flow analysis model for electronically coupled distributed energy resources," *IEEE Trans. Power Del.*, vol. 26, no. 2, pp. 899–909, 2011.

[21] P. Kundur, *Power System Stability and Control*. New York: McGraw-Hill, 1994.

[22] C. Concordia and S. Ihara, "Load Representation in Power System Stability Studies," *IEEE Trans. Power App. Syst.*, vol. PAS-101, no. 4, pp. 969–977, 1982.

[23] X. P. Zhang, "Fast three phase load flow methods," *IEEE Trans. Power Syst.*, vol. 11, no. 3, pp. 1547–1554, 1996.

[24] "STAMFORD Gennerator Technical Datasheet." [Online]. Available: https://stamford-avk.com/sites/default/files/literature/all/MVSI804R Wdg 51.pdf.

[25] M. A. Allam, A. A. Said, M. Kazerani, and E. F. El Saadany, "A Novel Dynamic Power Routing Scheme to Maximize Loadability of Islanded Hybrid AC/DC Microgrids under Unbalanced AC Loading," *IEEE Trans. Smart Grid*, vol. PP, no. 99, pp. 1–1, 2017.

[26] M. A. Allam, A. A. Hamad, M. Kazerani, and E. F. El-Saadany, "A steady-state analysis tool for unbalanced islanded hybrid AC/DC microgrids," *Elect. Power Syst. Res.*, vol. 152, pp. 71–83, 2017.

Mahmoud A. Allam (S'15) received his B.Sc with honors and M.Sc. degrees in electrical power engineering from Ain Shams University, Cairo, Egypt in 2009 and 2013, respectively. He is currently pursuing his Ph.D. degree in the Department of Electrical and Computer Engineering, University of Waterloo, Waterloo, ON, Canada.
His research interests include design and control of power electronic converters, distributed generation, renewable energy, and analysis, operation, and control of microgrids and smart distribution systems.

Amr A. Hamad (S'13, M'17) received the B.Sc. and M.Sc. degrees in electrical engineering from Cairo University, Giza, Egypt, in 2007 and 2010, respectively, and the Ph.D. degree in electrical and computer engineering from the University of Waterloo, Waterloo, ON, Canada, in 2016. He is currently a research associate with Measurement Sciences and Standards, National Research Council Canada. His research interests include planning of distribution systems, distributed and renewable generation, control of smart distribution systems, and the development of measurement techniques and instrumentation for accurate measurements of high-voltage active/reactive power and energy under difficult operating conditions.

Mehrdad Kazerani (S'88, M'96, SM'02) received his B.Sc., Master's and PhD degrees in Electrical Engineering from Shiraz University, Iran (1980), Concordia University, Canada (1990), and McGill University, Canada (1995), respectively. From 1982 to 1987, he was with the Energy Ministry of Iran. He is presently a Professor with the Department of Electrical and Computer Engineering, University of Waterloo, Waterloo, Ontario, Canada. He is a registered professional engineer in the province of Ontario. His research interests include current-sourced converter applications, power quality/active power filters, matrix converters, distributed power generation, utility interface of alternative energy sources, energy storage and battery charging systems, battery electric, hybrid electric and fuel cell vehicles, microgrids and FACTS.